RSC Advances

ROYAL SOCIETY OF CHEMISTRY

www.rsc.org/advances

Influence of particle size on performance of nickel oxide nanoparticle-based supercapacitor

Siamak Pilban Jahromi[a], Alagarsamy Pandikumar*[a], Boon Tong Goh[a], Yee Seng Lim[a], Wan Jefrey Basirun[b], Hong Ngee Lim[c] and Nay Ming Huang[a]*

[a]Low Dimensional Materials Research Centre, Department of Physics, Faculty of Science, University of Malaya, 50603 Kuala Lumpur, Malaysia

[b]Department of Chemistry, Faculty of Science, University of Malaya, 50603 Kuala Lumpur, Malaysia

[c]Department of Chemistry, Faculty of Science, Universiti Putra Malaysia, 43400 UPM Serdang, Selangor, Malaysia

*E-mail: pandikumarinbox@gmail.com and huangnayming@um.edu.my

Abstract

The influence of the particle size of an active material on its performance as a supercapacitor electrode was reported. NiO NPs with a uniform particle size were synthesized via a facile sol-gel method, and various sizes of NiO NPs (8, 12, and 22 nm) were achieved by calcination at various temperatures (300, 400, and 500 °C). TEM observations and XRD analysis were used to determine the particle size of the NiO NPs. The field emission scanning electron microscopy (FESEM) and transmission electron microscopy (TEM) images showed flake-like morphologies, which consisted of interconnected nanoparticles with a porous channel to facilitate the diffusion of the electrolyte. The NiO NPs with an average particle size of 8 nm gave the highest specific capacitance value of 549 Fg^{-1} at a scan rate of 1 mVs^{-1} compared to the NiO NPs with average particle sizes of 12 and 22 nm. These results suggest that the particle size of the NiO nanostructure plays an important role because of the presence of a higher number of active sites for a faradaic reaction.

1. Introduction

Sustainable energy resources are one of the most important research areas in the world today, for uninterrupted technology development. The growing energy crisis in recent decades is due to the rising cost of fossil fuels, depletion of fossil fuels, and growing concerns about environmental pollution and global warming [1]. However, many of these energy resources have their own challenges to overcome because of their intermittent characteristics. Therefore, an efficient energy storage method is a technological challenge to ensure the availability of energy [2]. The most promising electrical energy storage devices are conventional capacitors, electrochemical capacitors (ECs), batteries, and fuel cells. ECs, which are also known as supercapacitors, are considered to be an energy storage technology that can act as a bridging function for the energy/power gap between batteries/fuel cells, which have high energy storage, and conventional capacitors, which have high power output [3, 4]. There are two main mechanisms for ECs: (a) electrochemical double-layer capacitors (EDLCs), which have no electrochemical reaction during the charging and discharging processes, and (b) faradaic supercapacitors (FS) or pseudocapacitors, in which there is a faradaic redox reaction in the electrode/electrolyte interface. The remarkable performance of pseudocapacitor materials compared to that of the EDLC materials in supercapacitors open up new research possibilities, particularly in transition metal oxides like nickel oxide [5, 6].

Several alternative electrode materials have been investigated, including metal oxides, metal hydroxides, metal sulfides, conducting polymers, and carbonaceous materials [7-9]. Metal oxides such as RuO_2, Co_3O_4, MnO_2, and NiO are the most promising materials for pseudocapacitors because of their high specific capacitance. The pseudocapacitor properties of RuO_2 have attracted a great deal of attention because of their high electrochemical stability, wide potential

window, and high specific capacitance. However, the high cost of RuO_2 limits its commercial application. Hence, NiO is a promising alternative transition metal because it is easily available, has a low cost and good electrochemical stability, and is a p-type semiconductor, with a wide band-gap of 3.6–4.0 eV [10]. Recently, the advances in the synthesis of the NiO nanostructure have caused it to receive more attention. Furthermore, its outstanding theoretical specific capacitance of 3750 Fg^{-1} and thermal stability made NiO a viable choice for the construction of high-performance supercapacitors [11, 12]. Hence, much of the research has focused on the size controlled synthesis of tailored NiO nanostructures to improve the electrochemical properties and increase its specific capacitive [13, 14].

Several methods have been employed to synthesize NiO nanostructures, including pulse laser deposition (PLD) [15], sol–gel [16], solvothermal [10], hydrothermal [17], precipitation [18], sonochemical [19], anodic plasma [20], microemulsion [21], and thermal decomposition methods [22]. The preparation of NiO nanostructures is a complicated process, and a wide range of synthetic parameters affect the properties of the final products [15-22]. NiO with a porous structure and appropriate high specific surface area can facilitate a very short diffusion pathway for ions to connect with the external and internal electroactive sites and enhance the rate of faradaic redox reaction. Sol–gel synthesis is one of the simplest, most promising, and lowest-cost methods for preparing NiO NPs[23]. The sol–gel method has advantages such as producing a uniform morphology, high crystallite size and purity, and controllable particle size, which can improve the electrochemical properties of the NiO NPs as an electroactive material in the supercapacitors.

Several groups have reported the synthesis of flaky, porous nickel oxide to facilitate the diffusion of electrolyte to improve the electrochemical performance of nickel oxide [4, 11, 24]. In a previous report, Khairy et al. explored the influence of the morphology, surface area, and pore size/distribution of NiO nanostructures on the electrochemical energy storage performance [25]. However, to the best of our knowledge, there has been no report on the influence of the particle size of the NiO NPs forming the porous channel on the performance of a supercapacitor electrode. The diffusion of the aqueous electrolyte is aided if the channel is larger than the molecular sizes of the electrolyte ions. In this regard, the particle size of NiO NPs should be kept small, while maintaining the channel within its flaky structure. This subject has been overlooked by the research community. NiO NPs with average sizes of 8, 12, and 22 nm were synthesized through a sol–gel method in a gelatin medium followed by calcination at 300, 400, and 500 °C, respectively. The prepared NiO NPs with various particle sizes were characterized by XRD, FESEM, and TEM. The electrochemical performances of the NiO NPs with different particle sizes as electroactive materials for supercapacitors were studied in the presence of an electrolyte (1 M KOH).

2. Experimental Section

2.1. Preparation of NiO NPs

NiO NPs were synthesized using a sol–gel method as follows. Typically, 5 g of $Ni(NO_3)_2.6H_2O$ (Acros, 99%) was dissolved in 20 mL of deionized water and then stirred for 30 min. Meanwhile, 2 g of gelatine (type-B from bovine skin, Sigma Aldrich) was separately dissolved in 40 mL of deionized water, and then stirred for 30 min at 60 °C to obtain a clear gelatine solution. After that, the Ni^{2+} solution was added to the gelatine solution and heated in a

water bath at 80 °C under stirring. The stirring was continued for 15 h to obtain a viscous and bright green gel. This gel was rubbed on the inner side of a crucible. The bright green gel was then placed into a horizontal tube furnace (100 cm in length, 5 cm in diameter in the air at 1 atm of pressure). The furnace was heated from room temperature to 300, 400, or 500 °C at a rate of 30 °C/min. After being held at the final temperature for 1 h, the furnace was cooled down naturally to room temperature.

2.2. Material Characterization

The phase purity and crystallite size of the NiO NPs were characterized using XRD (Philips, X'pert, CuKα) with a radiation wavelength of λ = 1.54056 A°. TEM was carried out on a Hitachi-7100 transmission electron microscope to calculate the average particle sizes of the NPs. The morphologies of the samples were observed on a JSM-7600F FESEM operated at 5–20 KV.

2.3. Electrochemical Measurements

The NiO NP electrode was fabricated by mixing 75 wt% of the NiO NP powder with 15 wt% of acetylene black and 10 wt% polyvinylidene difluoride (PVdF) in 1-methyl-2-pyrrolidinone (NMP) as the solvent to produce a slurry. Then, one side of a cleaned nickel foil (0.125 mm thickness, 1 cm^2 area) was coated with the slurry and dried in a horizontal tube furnace at 90 °C for 12 h in air. The mass of NiO NPs coated on each electrode was approximately ~2 mg. A standard three-electrode system was used for electrochemical measurements. The NiO NP-coated Ni foil was used as the working electrode, while graphite and Hg/HgO were used as the counter and reference electrodes, respectively. Cyclic voltammetry (CV) at different scan rates; chronopotentiometry (CP) at different current densities; and

electrochemical impedance spectroscopy (EIS) with a frequency range of 100 KHz to 0.01 Hz, an AC amplitude of 5 mV, and a bias potential of 0.2 V, were carried out using a potentiostat (Versa STAT 3, AMETEK). All the experiments were carried out using a freshly prepared 1 M KOH solution as the electrolyte at room temperature.

3. Results and Discussion

3.1. X-ray Diffraction and Crystallite-size Analysis

The XRD patterns of the NiO NPs calcined at different temperatures are shown in Figure 1. All of the XRD patterns clearly show the diffraction peaks of the (111), (200), (220), (311), and (222) crystal planes, corresponding to the face-centered-cubic (fcc) structure of the NiO (JCPDS card No. 01-089-3493). The results also show that the synthesized NiO NPs had a high purity, with the absence of impurity peaks. It was observed that the intensity of the diffraction peaks increased with the calcination temperature, which indicated the better crystallinity of the nickel oxide formed at a higher calcination temperature.

Several techniques can be used to calculate the crystallite size, such as the Scherrer equation ($D=K\lambda/\beta \cos\theta$), where D is the grain size, K is the constant of the Scherrer formula related to an index (hkl) and the shape of the NPs, λ is the X-ray wavelength, θ is the XRD diffraction angle, and β is the full width at half maximum (FWHM) of the diffraction peak measured in radians. From the Scherrer equation, parameter β needs to be corrected because the width of the broadening peaks is the result of both the crystallite size and micro-structure strain. In order to correct β for β_D, the Gaussian equation is used to separate the effects of the crystallite size and micro-structure strain, as shown in Equation 1 [26].

$$\beta_D = \left(\beta^2 - \beta^2_{standard}\right)^{\frac{1}{2}} \quad 1$$

Because of the limitation of the Scherrer equation, in our study, the Williamson–Hall plotting method was used to study the crystallite size and micro-structure strain effects. In this method, we consider that these effects contribute to the line broadening, which can be separated using the Lorentzian equation, as shown in Equation 2.

$$\beta_{hkl} = \beta_D \pm \beta_\varepsilon \quad 2$$

where β_D is the width of the diffraction peak caused by the particle size, β_ε is the width of the diffraction caused by the micro-strain, and β is the full line width corrected for instrumental effects. The positive and negative signs indicate lattice expansion and lattice compression, respectively [27]. However, a better evaluation of the size-strain factors in the case of isotropic line broadening can be obtained by considering an average size-strain plot (SSP), which gives less weight to data obtained from reflections at high angles, where the accuracy is usually lower. In this approximation, it is assumed that the crystallite size and the strain profile are described by Lorentzian and Gaussian functions, respectively. The total peak broadening is obtained from Equation 3.

$$(d_{hkl}\beta_{hkl}\cos\theta)^2 = \frac{A}{D}\left(d^2_{hkl}\beta_{hkl}\cos\theta\right) + \left(\frac{\varepsilon}{2}\right)^2 \quad 0$$

3

The constant A depends on the shape of the particles [28]. In Figure 2, the term $(d_{hkl}\beta_{hkl}\cos\theta)^2$ is plotted with respect to $\frac{A}{D}(d^2_{hkl}\beta_{hkl}\cos\theta)$ for all of the diffraction peaks of the NiO NPs with the cubic phase from 2θ = 20° to 80°. In this case, the crystallite size is determined from the slope of the linearly fitted data, where the root of the y-intercept gives the strain. The results obtained from the SSP models are summarized in Table 1. It can be clearly seen that the crystallite size of the NiO NPs increased with the increasing calcination temperature.

Furthermore, the lattice constant decreased because of the increase in the size of the particles and thus decreased the micro-strain. Although the effect of the particle size on the lattice constant has been noted, the real facts are unclear. Some authors have assumed that it is a consequence of the Laplace pressure, $\Delta P = 2\delta/r$, where δ is the surface tension, and r is the diameter of the NPs. In addition, the concentration of vacancies might affect the size of the lattice constant [29].

3.2. Morphological Studies

The morphologies and structures of the NiO NP samples with various calcination temperatures are shown in Figures 3. The FESEM images (Figure 3(a-c)) show a flake-like morphology for the NiO NPs samples, with a porous open channel within the flake morphology. The porous channel formed inside the flaky morphology of the nickel oxide is due to the evaporation of water molecules and decomposition of chemically bonded groups [23]. Moreover, the images clearly indicate that the flaky morphology grows rapidly with an increase in the calcination temperature. These observations are in good agreement with a previous report [24]. From Figure 3d, a compact channel with particularly small pores is obtained at 300 °C, where smaller nickel oxide particles can pack closer to each other, forming a very narrow channel within the flaky structure. When the calcination temperature increases (Figure 3e-f), the growth of the crystallite size of the nickel oxide, which formed larger and rougher particles, made the close packing of the nickel oxide difficult. Hence, a larger channel was formed within the flaky structure. The histograms for the size distribution of the NiO NPs were measured and are given in Figure 3(g-i). These show that the average particle sizes of the NiO NPs were 8, 12, and 22 nm when calcined at 300, 400, and 500 °C respectively. The mean particle sizes estimated from the TEM micrographs are in good agreement with the results of the XRD analysis.

The formation mechanism of the flake-like NiO structure involves three steps: nucleation, growth, and oriented attachment. The nucleation process is strongly dependent on the degree of super-saturation. In the nucleation process, the super-saturation is very high, and the electrostatic repulsive barriers are low. Hence, the particles tend to aggregate with one another. In the second step, the agglomeration of primary NiO NPs (formed at low temperature) plays an important role in the growth of the NiO NPs calcined at a higher temperature. The coalescence of the primary particles in the agglomerates led to the elimination of primary particles below 10 nm in size due to the higher calcination temperature. The smaller primary particles tend to be connected together. This phenomenon gives rise to larger agglomerated particles, along with the rapid minimizing of the interfacial free energy, which is proportional to $2\gamma/R$, where R is the radius of the spherical particles, and γ is the specific interfacial free energy [30]. In the attachment step, it is well known that the surface energy reduction is the principle rule for crystal growth, and the morphology progression is promoted by a greater decrease in the surface energy [31]. It is conceivable that the attachment of the NiO NPs along a particular direction to form a flake-like structure is due to the tendency toward minimum surface energy.

Figure 4 shows the crystallite and particle size as a function of temperature. In this case, the particle growth was greater than the crystal growth, which shows that the agglomeration of primary NiO NPs (formed at low temperature) plays an important role in the growth of NiO NPs that are calcined at a higher temperature. The NiO samples calcined at 400 and 500 °C showed larger particle sizes with wider size distributions compared to the NiO sample calcined at 300 °C.

3.3. Influence of Particle Size on Electrochemical Behavior

Cyclic voltammetry (CV) was used to investigate the electrochemical properties of the NiO NPs synthesized via the sol–gel method as electrode materials for supercapacitors in the presence of 1 M KOH. Figure 5 shows the cyclic voltammograms observed for the NiO NPs with different average particle sizes of 8, 12, and 22 nm calcined at 300, 400, and 500 °C, respectively, at scan rates of 1, 5, 15, 20, 30, 40 and 50 mVs^{-1}. The CV curves show a similar trend, but differ only in the current density magnitude and potential window. Two strong peaks are shown, which correspond to the typical pseudocapacitance behavior due to the occurrence of the faradaic redox reactions within the system. The oxidation peak was due to the conversion of NiO to NiOOH, while the reduction peak was due to the reverse reaction. The charge storage of the NiO NP electrode arises from the following redox reaction.

$$NiO + zOH^- \leftrightarrow zNiOOH + (1-z)NiO + ze^- \quad (4)$$

The choice of the potential window in a suitable range is important to obtain well-resolved redox peaks [32, 33]. This strategy is also helpful to study the NiO NP size effect as an electroactive material for pseudocapacitors. Figure 5 shows CV patterns of the NiO NP electrodes at different scan rates. The current density of the redox process increases with the scan rate. The anodic peak shifts toward the positive region, and the cathodic peak shifts toward the negative region. The behaviors of the NiO electrodes are in good agreement with previous reports [34-38]. The observed shifts in the redox peaks are attributed to a rapid ion/electron diffusion rate at the interface/surface structure of the NiO NP electrodes during the faradaic redox reaction [32].

The capacitive properties of pseudocapacitors are based on the surface reversible redox mechanism. The redox peak potentials in the CV patterns are indicated as E_a and E_c, respectively. The asymmetry in the redox peaks of the NiO NP electrodes indicates a kinetic irreversibility during the faradaic reaction. A smaller $\Delta E = E_a - E_c$ value shows better reversibility in the redox process[5]. Hence, at lower scan rates, the NiO NP electrodes show better reversibility in the faradaic reaction (Figure 5). From Figure 5d, among the three NiO NP electrodes, the reversibility of the redox process increases with the calcination temperature. NiO NPs with a calcination temperature of 500 °C had an average size of 22 nm, showing the best redox reversibility, followed by NiO NPs calcined at 400 °C and 300 °C, which had average sizes of 12 and 8 nm, respectively. This was due to the higher cyrstalinity for the NiO NPs calcined at 500 ºC and it showed a better reversibility. In addition, the FESEM images show that the nano-flake morphology at 300 °C with a particle size of 8 nm changed to a macro-flake morphology at 500 °C with a particle size of 22 nm, which indicated that the overall structure was more robust and less susceptible to changes in its structure. From the comparison of the NiO NP electrode CV curves (Figure 5d) for different particle sizes under the same electrochemical conditions (scan rate of 30 mV s^{-1} & 1 M KOH), it can be seen that at a higher calcination temperature with a larger particle size, the magnitude of the current density decreases, and the reversibility increases.

To maximize the faradaic reaction processes, a nanostructure with an open channel is preferred because of the presence of electroactive outer and inner pores. This approach maximizes the pseudocapacitve contribution of the redox active nickel oxide [38]. Several methods

have been used to synthesize various open structures for active electrode materials. However, the influence of the size of the particles that form the open porous structure on the electrochemical performance has not been reported. The inset of Figure 5d shows the linear relationship between the anodic peak current density and the scan rate (quasi-linear) for NiO NP electrodes with average sizes of 8, 12, and 22 nm. Based on this plot, the slope of the linear data is proportional to the surface reaction of the NiO NP electrodes [39]. The results showed that the surface faradaic reaction of the NiO NP electrodes decreases when the particles size increases. Although a large electrolyte channel with a suitable pore size plays an important role in facilitating the diffusion of the electrolyte, the size of the particles forming the channel is critically important to maintain a high number of active sites for the faradaic reaction. As shown in the TEM images (Figure 3d-f), increasing the calcination temperature created a larger electrolyte channel with larger particles of nickel oxide, leading to fewer active sites for the redox reaction to occur. Hence, the surface reaction was decreased, as shown in the inset of Figure 5d.

The specific capacitances (C_s) of the NiO NP electrodes were calculated based on the CV curves using Equation 5.

$$C_s = \frac{1}{vm.\Delta V_{if}} \int_{V_i}^{V_f} I \times V dV \qquad 5$$

where C_s is the specific capacitance of the NiO sample (F g^{-1}), v is the scan rate (V s^{-1}), m is the mass of NiO NPs used as the active material (g), ΔV_{if} is the applied potential window (V_i to V_f), and the integral term is equal to the area under the CV curve. The calculated specific capacitance values for NiO NPs with particle sizes of 8, 12, and 22 nm were 548, 442, and 199 Fg^{-1},

respectively, at a scan rate of 1 mVs^{-1}. Figure 6 shows the capacitance values of the NiO electrodes calculated at different scan rates from 1 to 50 mVs^{-1}. The results showed that the 8-nm NiO NPs exhibited the highest specific capacitance at all the scan rates. The NiO NPs showed the best performance because of the small particle size and narrow size distribution, with the nickel oxide closely packed together to form a flake-like morphology, which contributed to a high degree of electrolyte channel with a high number of redox active sites. This structure allowed the pseudocapacitace from the nickel oxide to be fully harnessed, and thus exhibited a superior charge storage performance in the supercapacitor application. Conversely, when large particles of nickel oxide were packed loosely, they formed a much more porous electrolyte channel. However, the lower number of redox active sites made it undesirable for fast ion kinetics and decreased the charge storage performance. Table 2 summarizes the reversibility, specific capacitance of the NiO NPs with different particles at various scan rate. It can be seen that, the NiO NPs with 22 nm showed good reversibility and NiO NPs with 8 nm showed high specific capacitance value.

Chronopotentiometry is a method used to investigate the stability, charge/discharge ability, and energy/power density. Figure 7 shows the charge/discharge curves of the NiO electrodes with particle sizes of 8, 12, and 22 nm. Charge/discharge measurements were carried out at various current densities in 1 M KOH. The potential value reached the maximum for all the NiO samples while employing the different current densities. It was found that the charge/discharge time decreased and the potential values increased for all the samples with an increase in the current density. The nonlinear charge/discharge curves confirmed the

pseudocapacitance behavior of the NiO NP electrodes, which was in close agreement with the CV results, including the presence of redox peaks [40].

The accessibility of ions through the porous channel of the electroactive material is vital for an efficient faradaic reaction mechanism. In addition, the particle size is an important parameter to maximize the faradaic contribution of the electroactive materials [41-44]. Figure 8(a and b) compares the charge/discharge curves of the NiO NP electrodes at low and high current densities under the same electrochemical conditions (current density 0.1 and 1 Ag^{-1} & 1 M KOH). It can be seen that the structure of the NiO NP electrode affects the charge/discharge time and potential window [45]. The results showed that the NiO electrode with an average size of 8 nm had a longer charge/discharge time than the other samples. This could be attributed to the smaller particle size and nano-flake structure, which rendered a higher specific surface area for the 8-nm NiO NP electrode.

The schematics in Figure 8(c-d) explain the effect of the size and morphology on the ionic diffusion into the NiO electrodes. When the current density is low, the OH^- ions have sufficient time to penetrate into the inner-pore surface of the NiO electrodes. This effect contributes to a lower resistance between the electrolyte/ions and the NiO structure. Figure 8(a-b) shows the potential windows of the NiO NP electrodes, which are proportional to the current density. Figure 8(c-d) shows the effects of the charge/discharge at lower and higher current densities toward the electrolyte ion concentration at the electrode/electrolyte interface [45]. As seen, the ionic concentration at the electrode/electrolyte interface is proportional to the potential window in the supercapacitor.

The specific capacitances (C_s) of the NiO NP electrodes are calculated from the galvanostatic charge-discharge curves using Equation 6.

$$C_s = \frac{I \times \Delta t}{\Delta v_{if} \times m} \quad (4)$$

Here, C_s is the specific capacitance of the NiO electrode (Fg^{-1}), I is the current (A), m is the mass of the NiO as the active material (g), ΔV_{if} is the potential window (V_i to V_f), and Δt is the discharge time (S). The specific capacitance (C_S) values for the NiO electrodes with average sizes of 8, 12, and 22 nm are 379, 250, and 97 Fg^{-1} at 0.1 Ag^{-1} in 1 M KOH, respectively. Table 3 lists the specific capacitance values of the NiO NP electrodes at different current densities based on the charge/discharge curves. The results show that the NiO electrode with the average size of 8 nm also has the maximum discharge time for all the current densities. Therefore, it exhibits the highest specific capacitance for all the current densities in comparison to other electrodes (Table 3). These results are in good agreement with the capacitance behaviors obtained from the CV curves.

3.4. Influence of Particle Size on Capacitance Retention

The capacitance retention is an important characteristic that indicates the practically of an electrode material for supercapacitor applications. A life cycle study of the NiO NP electrodes with different particle sizes was carried out in a potential window of 0.0–0.6 V at a current density of 2.0 Ag^{-1}. Figure 9 shows the specific capacitance retention values of the NiO electrodes with different particle sizes over 1000 cycles. The capacitance retention values of the

NiO NP electrodes with particle sizes of 8, 12, and 22 nm after 1000 charge/discharge cycles at a current density of 2.0 Ag^{-1} were 60.6%, 72.9%, and 81.8%, respectively. The NiO NP electrode with a particle size of 22 nm exhibited the highest stability because the larger particles and better crystallinity of the nickel oxide formed a much more robust physical structure that inhibited the gradual structural deterioration of the electrolyte channel resulting from the repetitive diffusion and effusion in the electrolyte channel [25].

Based on the galvanostatic charge/discharge curves, the energy and power densities can be calculated using Equations 7 and 8, respectively, as follows:

$$D_e = C(\Delta V)^2/2 \quad (5)$$

$$D_p = De/\Delta t \quad (6)$$

Here, D_e is the energy density, C is the specific capacitance, ΔV is the potential discharge window, D_p is the power density, and Δt is the discharge time in the potential window. Figure 10 shows the energy and power density values of the NiO NP electrodes at different current densities, based on the charge/discharge curves. The 8-nm NiO NPs exhibited the highest energy density and power density. The energy densities of the 8-nm NiO NPs were 17.8, 13.4, 11.3, and 11.0 $Wh(kg)^{-1}$ and the power densities were 29.1, 59.7, 153.6, and 321.7 $W(kg)^{-1}$ at current densities of 0.1, 0.2, 0.5, and 1.0 Ag^{-1}, respectively. The Ragone plot result (Figure 10) is in good agreement with those for similar previously reported systems [32, 46]. These results indicate that the 8-nm NiO NPs are more suitable for supercapacitor applications compared to the other samples because of the high accessibility of the OH^- ions to the outer and inner pore surface at different current densities.

The impedance plots shown in Figure 11 are divided into a high-frequency region (partial semicircle) and low-frequency region (straight slope line) with the transition between the two regions called the "knee frequency." The internal resistance of the electrode materials, resistance of the electrolyte, and contact resistance between the electrode and current collector are factors that affect the capacitance. The diameter of the semicircle in the high-frequency region corresponds to the faradaic charge-transfer resistance (R_{ct}) [47]. From Figure 11, the charge-transfer resistance of the NiO NP electrodes are reciprocal to the particle size, in the following order: 22 < 12 < 8 nm (Figure 11 inset). The low charge-transfer resistance is one of the reasons for the better crystallinity of the 22-nm NiO NP electrode with the macro-flake morphology compared to the other NiO electrodes [25]. The Nyquist plot after the knee frequency has a straight line slope in the low-frequency region. For a resistor and capacitor in series, the Nyquist plot in the lower frequency range definitely shows a finite slope, which represents the diffusion resistance (Warburg impendence, W) of the electrolyte ion diffusion in the pore structure of the electrode materials. The diffusion line of the 22-nm NiO NPs indicates that the material has low diffusion resistance because of the highly open channel structure.

4. Conclusion

In this work, the size effect of NiO NPs on the electrochemical performance was studied. Various sizes of NiO NPs (8, 12, and 22 nm) were synthesized via a facile sol–gel method using gelatine as a green polymerizing agent, followed by calcination at various temperatures (300, 400, and 500 °C). The calcination temperature played an important role in controlling the particle size. The NiO NPs with different size distributions were used as electroactive materials in supercapacitors, and their electrochemical behaviors were investigated by cyclic voltammetry, galvanostatic charge/discharge, and electrochemical impedance spectroscopic techniques in 1 M

KOH. The NiO NPs with an average particle size of 8 nm gave the highest specific capacitance value of 549 Fg^{-1} at a scan rate of 1 mVs^{-1} compared to those of the NiO NPs with average particle sizes of 12 and 22 nm. The NiO NPs with a 22-nm size showed good reversibility compared to the other NiO NPs because of the high crystalline nature when calcined at 500 °C. Further, the effects of the porous structure and size distribution of the NiO NPs on the supercapacitor performance such as the specific capacitance, current density, potential window, and energy/power density were also explored in this investigation. The study demonstrated that by controlling the size and morphology of a NiO NP film, it could be an ideal electroactive material for energy conversion and storage devices.

Acknowledgments

This work was financially supported by a High Impact Research Grant (UM.C/625/1/HIR/MOHE/05) from the Ministry of Higher Education Malaysia and UMRG program grant (RP007C/13AFR) and Exploratory Research Grant Scheme (ERGS) of ER003-2013A from the University of Malaya.

References:

1. Y.-Y. Yang, Z.-A. Hu, Z.-Y. Zhang, F.-H. Zhang, Y.-J. Zhang, P.-J. Liang, H.-Y. Zhang and H.-Y. Wu, *Mater. Chem. Phys.*, 2012, **133**, 363-368.
2. C. Liu, F. Li, L. P. Ma and H. M. Cheng, *Adv. Mater.*, 2010, **22**, E28-E62.
3. C. Largeot, C. Portet, J. Chmiola, P.-L. Taberna, Y. Gogotsi and P. Simon, *J.Am. Chem. Soc.*, 2008, **130**, 2730-2731.
4. M. Fan, B. Ren, L. Yu, Q. Liu, J. Wang, D. Song, J. Liu, X. Jing and L. Liu, *CrystEngComm*, 2014, **16**, 10389-10394.

5. S. K. Meher, P. Justin and G. R. Rao, *ACS Appl. Mater. Interfaces*, 2011, **3**, 2063-2073.

6. G. P. Wang, L. Zhang and J. J. Zhang, *Chem. Soc. Rev.*, 2012, **41**, 797-828.

7. J. P. Liu, C. W. Cheng, W. W. Zhou, H. X. Li and H. J. Fan, *Chem. Commun.*, 2011, **47**, 3436-3438.

8. X. M. Liu and W. L. Gao, *Nanosci. Nanotechnol. Lett.*, 2011, **3**, 805-808.

9. G.-W. Yang, C.-L. Xu and H.-L. Li, *Chem. Commun.*, 2008, 6537-6539.

10. K. Anandan and V. Rajendran, *Mater. Sci. Semicond. Processing*, 2011, **14**, 43-47.

11. S.-I. Kim, J.-S. Lee, H.-J. Ahn, H.-K. Song and J.-H. Jang, *ACS Appl. Mater. Interfaces*, 2013, **5**, 1596-1603.

12. G. Wang, L. Zhang and J. Zhang, *Chem. Soc. Rev.*, 2012, **41**, 797-828.

13. M. Yang, J. X. Li, H. H. Li, L. W. Su, J. P. Wei and Z. Zhou, *Phys. Chem. Chem. Phys.*, 2012, **14**, 11048-11052.

14. S. K. Meher, P. Justin and G. R. Rao, *Nanoscale*, 2011, **3**, 683-692.

15. S. P. Jahromi, N. M. Huang, A. Kamalianfar, H. N. Lim, M. R. Muhamad and R. Yousefi, *J. Nanomater.*, 2012.

16. Q. Li, L. S. Wang, B. Y. Hu, C. Yang, L. Zhou and L. Zhang, *Mater. Lett.*, 2007, **61**, 1615-1618.

17. M. Zhou, H. Chai, D. Jia and W. Zhou, *New J. Chem.*, 2014, **38**, 2320-2326.

18. X. Xin, Z. Lu, B. Zhou, X. Huang, R. Zhu, X. Sha, Y. Zhang and W. Su, *J. Alloys Compounds*, 2007, **427**, 251-255.

19. A. Aslani, V. Oroojpour and M. Fallahi, *Appl. Surf. Sci.*, 2011, **257**, 4056-4061.

20. H. Qiao, Z. Wei, H. Yang, L. Zhu and X. Yan, *J. Nanomater.*, 2009.

21. T. Ahmad, K. V. Ramanujachary, S. E. Lofland and A. K. Ganguli, *Solid State Sci.*, 2006, **8**, 425-430.

22. F. Davar, Z. Fereshteh and M. Salavati-Niasari, *J. Alloys Compounds*, 2009, **476**, 797-801.

23. S. P. Jahromi, N. M. Huang, M. R. Muhamad and H. N. Lim, *Ceramics International*, 2013, **39**, 3909-3914.

24. S. Vijayakumar, S. Nagamuthu and G. Muralidharan, *ACS Appl. Mater. Interfaces*, 2013, **5**, 2188-2196.

25. M. Khairy and S. A. El-Safty, *RSC Adv.*, 2013, **3**, 23801-23809.

26. A. K. Zak, W. H. A. Majid, M. E. Abrishami and R. Yousefi, *Solid State Sci.*, 2011, **13**, 251-256.

27. N. S. Goncalves, J. A. Carvalho, Z. M. Lima and J. M. Sasaki, *Mater. Lett.*, 2012, **72**, 36-38.

28. A. K. Zak, R. Yousefi, W. H. Abd Majid and M. R. Muhamad, *Ceramics International*, 2012, **38**, 2059-2064.

29. A. I. Gusev and A. A. Remple, 2004.

30. A. Weibel, R. Bouchet, F. Boulc'h and P. Knauth, *Chem. Mater.*, 2005, **17**, 2378-2385.

31. R. L. Penn and J. F. Banfield, *Geochim. Cosmochim. Acta*, 1999, **63**, 1549-1557.

32. K. Liang, X. Z. Tang and W. C. Hu, *J. Mater.Chem.*, 2012, **22**, 11062-11067.

33. V. Ruiz, S. Roldán, I. Villar, C. Blanco and R. Santamaría, *Electrochim. Acta*, 2013.

34. A. D. Su, X. Zhang, A. Rinaldi, S. T. Nguyen, H. Liu, Z. Lei, L. Lu and H. M. Duong, *Chem. Phys. Lett.*, 2013, **561–562**, 68-73.

35. B. Ren, M. Fan, Q. Liu, J. Wang, D. Song and X. Bai, *Electrochim. Acta*, 2013, **92**, 197-204.

36. J. H. Zhu, J. A. Jiang, J. P. Liu, R. M. Ding, H. Ding, Y. M. Feng, G. M. Wei and X. T. Huang, *J. Solid State Chem.*, 2011, **184**, 578-583.

37. X. Cao, Y. J. Xu and N. Wang, *Sens. Actuator B-Chem.*, 2011, **153**, 434-438.

38. S. K. Meher, P. Justin and G. R. Rao, *Electrochim. Acta*, 2010, **55**, 8388-8396.

39. M. R. Mahmoudian, Y. Alias and W. J. Basirun, *Electrochim. Acta*, 2012, **72**, 53-60.

40. H. Jiang, T. Sun, C. Li and J. Ma, *RSC Adv.*, 2011, **1**, 954-957.

41. P. Simon and Y. Gogotsi, *Nature Mater.*, 2008, **7**, 845-854.

42. C. Yuan, B. Gao, L. Su and X. Zhang, *J. Colloid Interf. Sci.*, 2008, **322**, 545-550.

43. C. Yuan, X. Zhang, L. Su, B. Gao and L. Shen, *J. Mater. Chem.*, 2009, **19**, 5772-5777.

44. M.-W. Xu, S.-J. Bao and H.-L. Li, *J. Solid State Electrochem.*, 2007, **11**, 372-377.

45. P. M. Biesheuvel, Y. Q. Fu and M. Z. Bazant, *Phys. Rev. E*, 2011, **83**.

46. Y. Q. Zhang, X. H. Xia, J. P. Tu, Y. J. Mai, S. J. Shi, X. L. Wang and C. D. Gu, *J. Power Sources*, 2012, **199**, 413-417.

47. P. Justin, S. K. Meher and G. R. Rao, *J. Phys. Chem. C*, 2010, **114**, 5203-5210.

Tables

Table 1 Geometric parameters of NiO NPs calcinated at 300, 400, and 500 °C.

Calcination Temperature	Average Particle size (nm)$\pm\mathbf{0.2}$	Constant Lattice (A^0)	Size–strain plot D (nm)	Strain	Band gap (eV)
300℃	8.1	4.181	6.8	0.024	3.68
400℃	11.9	4.181	8.4	0.017	3.65
500℃	21.8	4.179	14.3	0.008	3.61

Table 2. Potential difference between redox peaks for NiO NPs at different calcination temperatures.

Scan Rate mVs^{-1}	NiO-8 nm		NiO-12 nm		NiO-22 nm	
	$\Delta E = E_a - E_c$ mV	C_s (F/g)	$\Delta E = E_a - E_c$ mV	C_s (F/g)	$\Delta E = E_a - E_c$ mV	C_s (F/g)
1	202	549	151	442	91	199
5	291	413	231	286	160	169
15	440	269	363	210	214	134
20	490	236	379	200	231	128
30	595	200	390	179	270	118
40	679	175	401	168	288	111
50	733	161	414	159	315	104

Table 3, The potential window, discharge time of NiO samples that produced at different calcination temperatures.

Current Density A/g	NiO NPs-8n m			NiO NPs-12 nm			NiO NPs-22 nm		
	ΔV (mV)	Δt (S)	D_E (Wh/Kg)	ΔV *(mV)*	Δt (S)	D_E (Wh/Kg)	ΔV *(mV)*	Δt (S)	D_E (Wh/Kg)
0.1	581	2200	17.8	593	1480	12.2	633	610	5.6
0.2	595	810	13.4	605	712	11.9	650	313	5.7
0.5	614	265	11.3	626	214	9.3	692	97	4.6
1.0	642	123	11.0	645	100	9.0	705	38	3.8

Figures and Caption

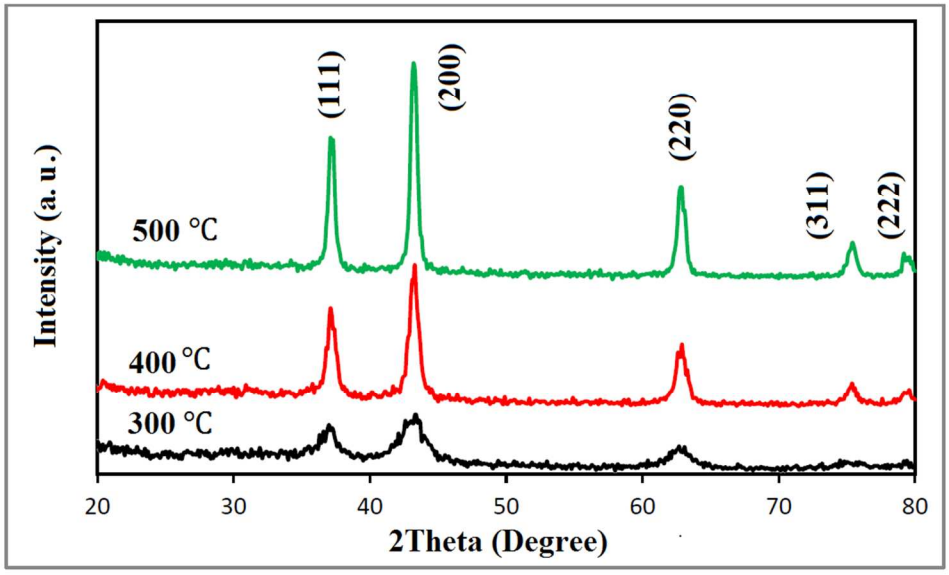

Figure 1. X-ray diffraction patterns of NiO NPs calcinated at different temperatures.

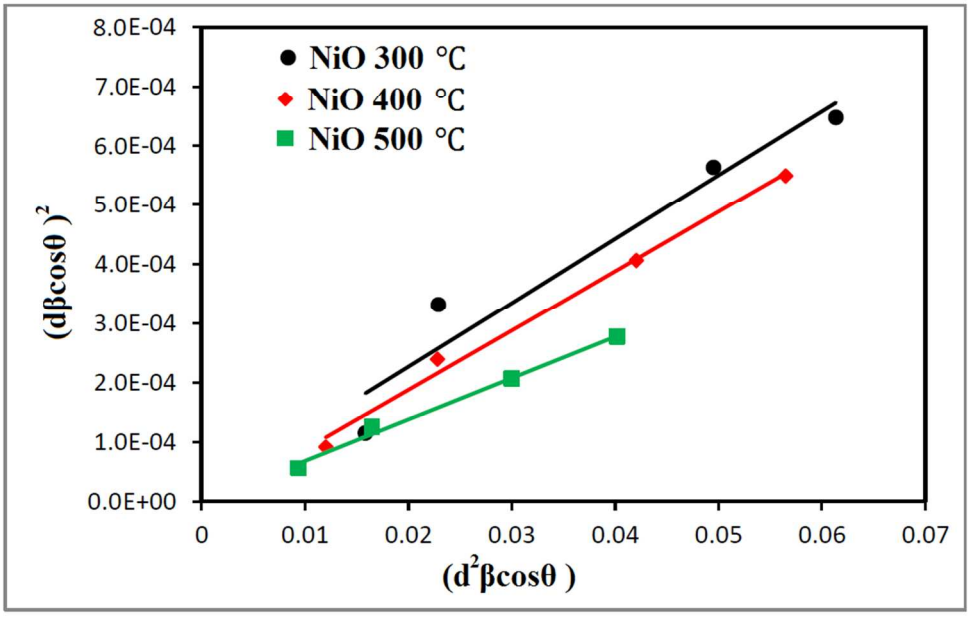

Figure 2. SSP plots of NiO NPs calcinated at different temperatures.

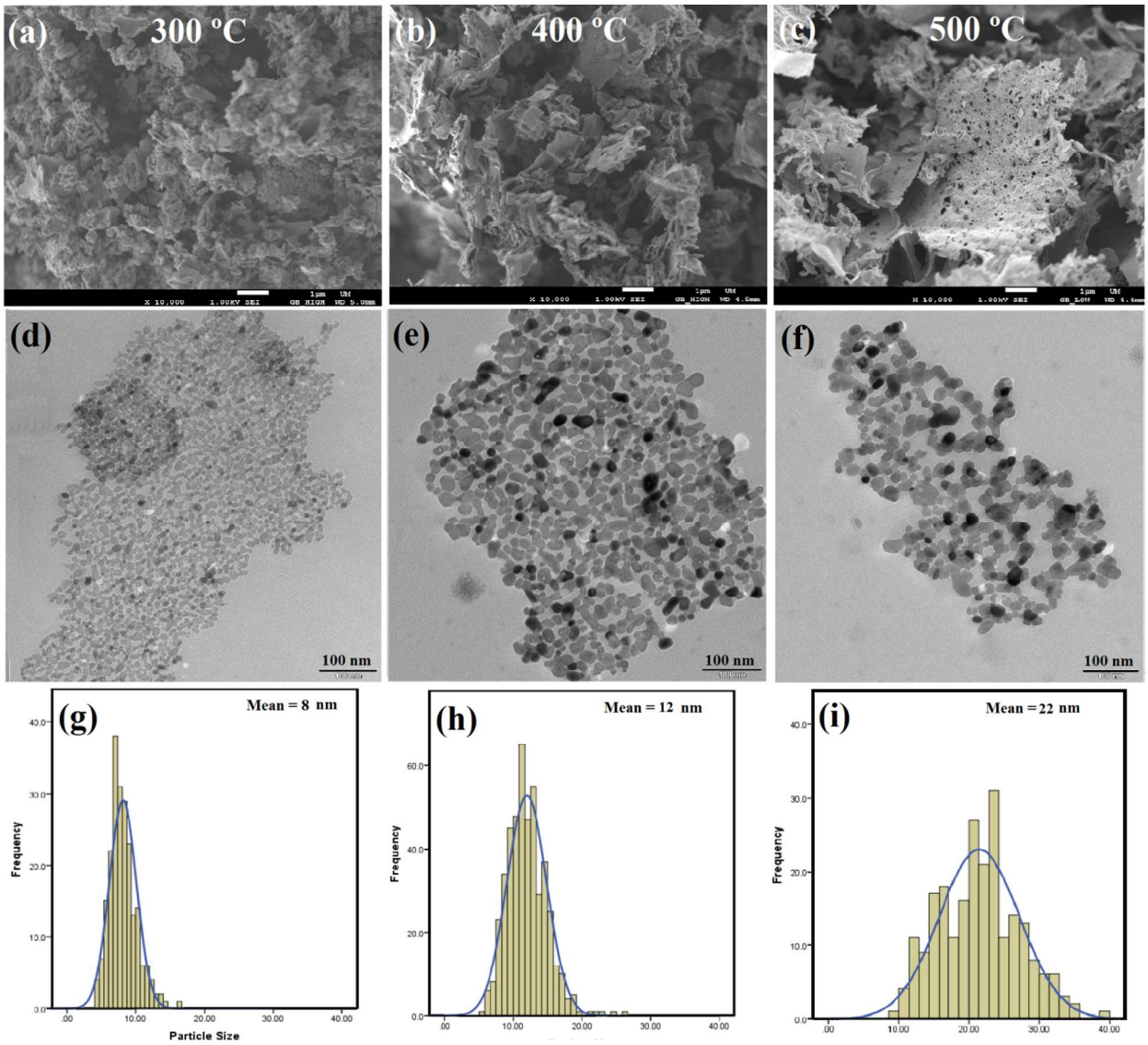

Figure 3. (a-c) FESEM morphological structures of NiO samples at different calcination temperatures. (d-f) TEM micrographs and (g-i) the size distribution of NiO NPs calcinated at different temperature.

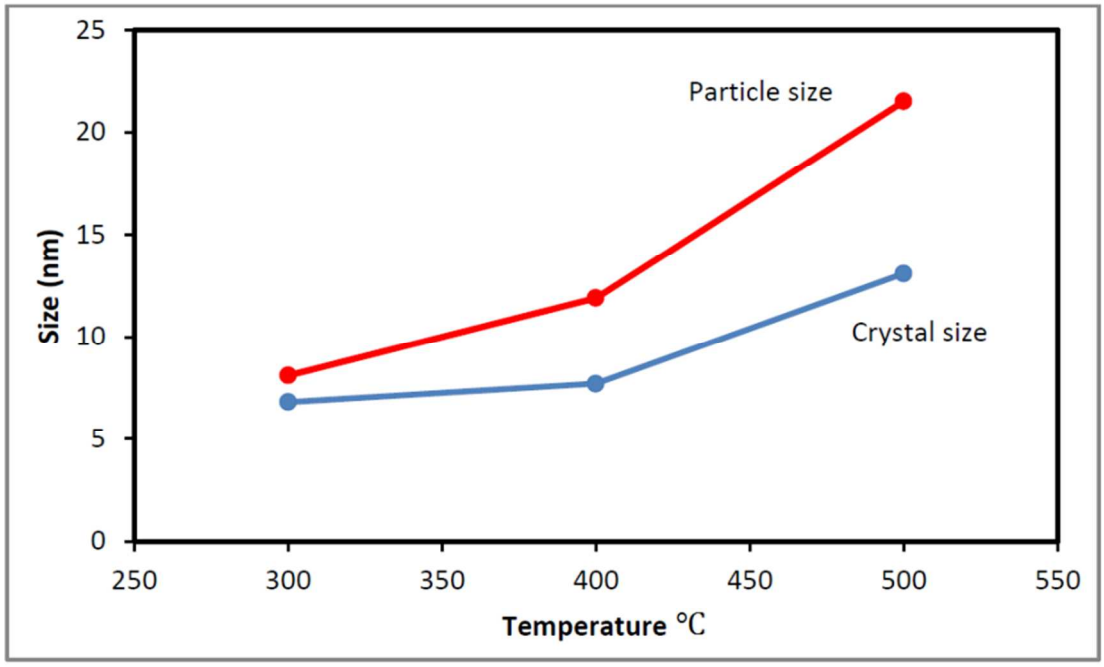

Figure 4. Plots obtained for the crystallite size and particle size of NiO NPs *vs.* calcination temperature.

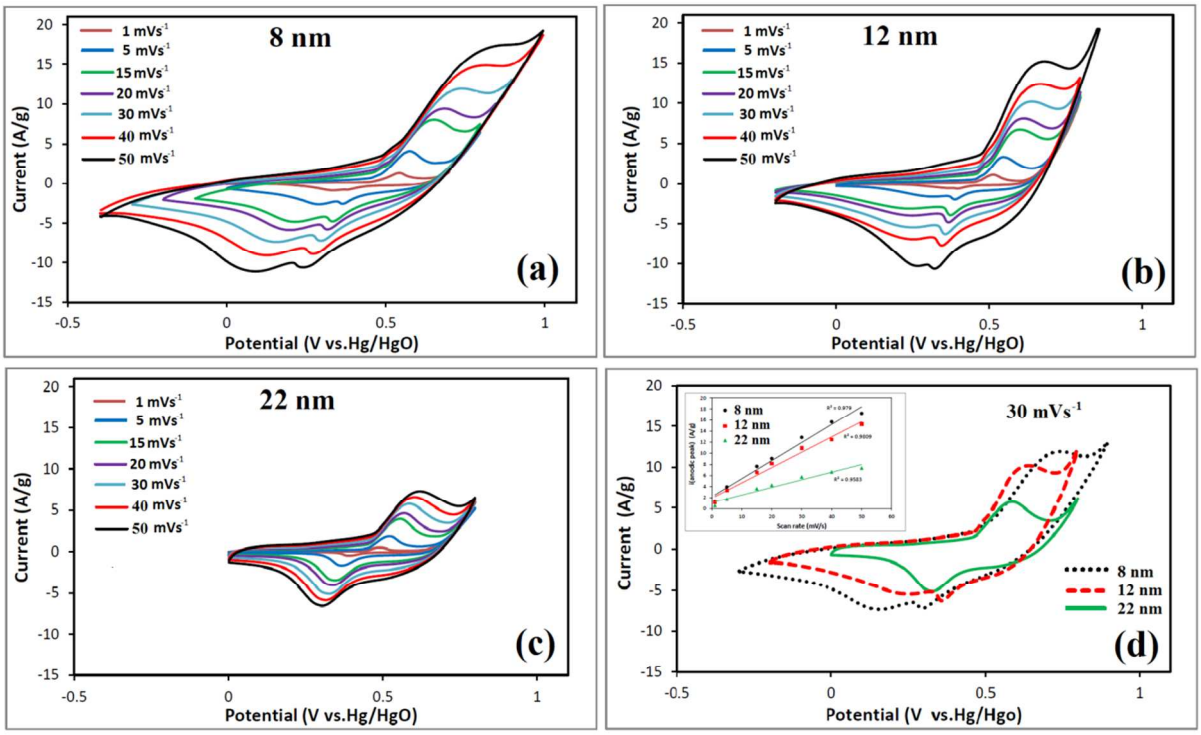

Figure 5. (a-c) Cyclic voltammograms obtained for the 8, 12, and 22 nm sized NiO NPs electrodes at different scan rate in the presence of 1 M KOH. (d) Cyclic voltammograms of NiO NPs with different particles size at the scan rate of 30 mVs^{-1} in 1 M KOH. Inside (d) Linear relationship between anodic current density and scan rate obtained for the NiO NPs with different particle size.

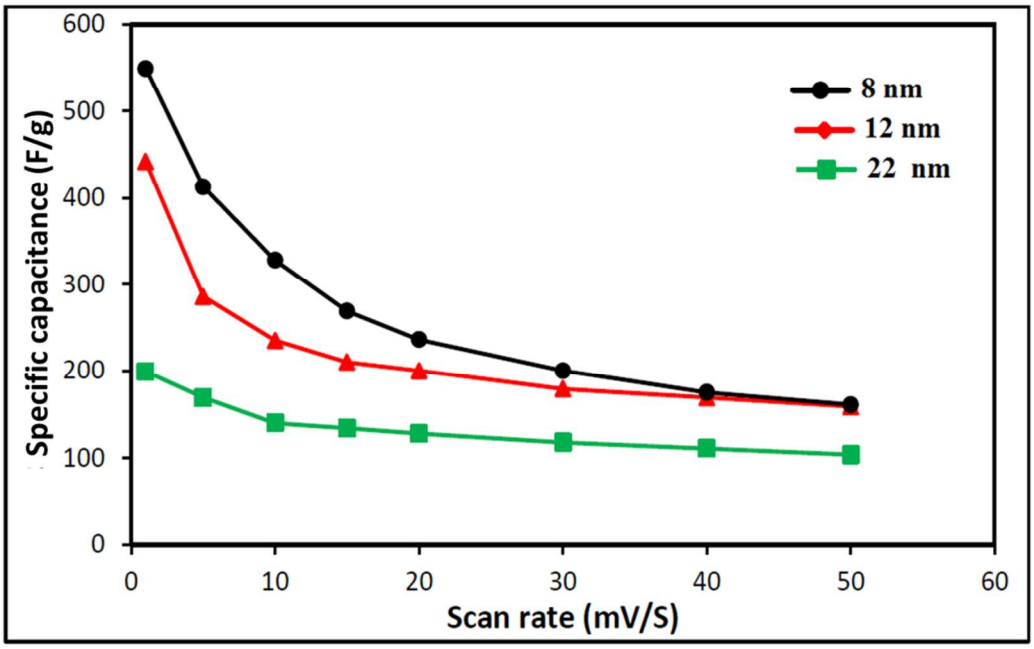

Figure 6. Specific capacitance of NiO NPs at different scan rate.

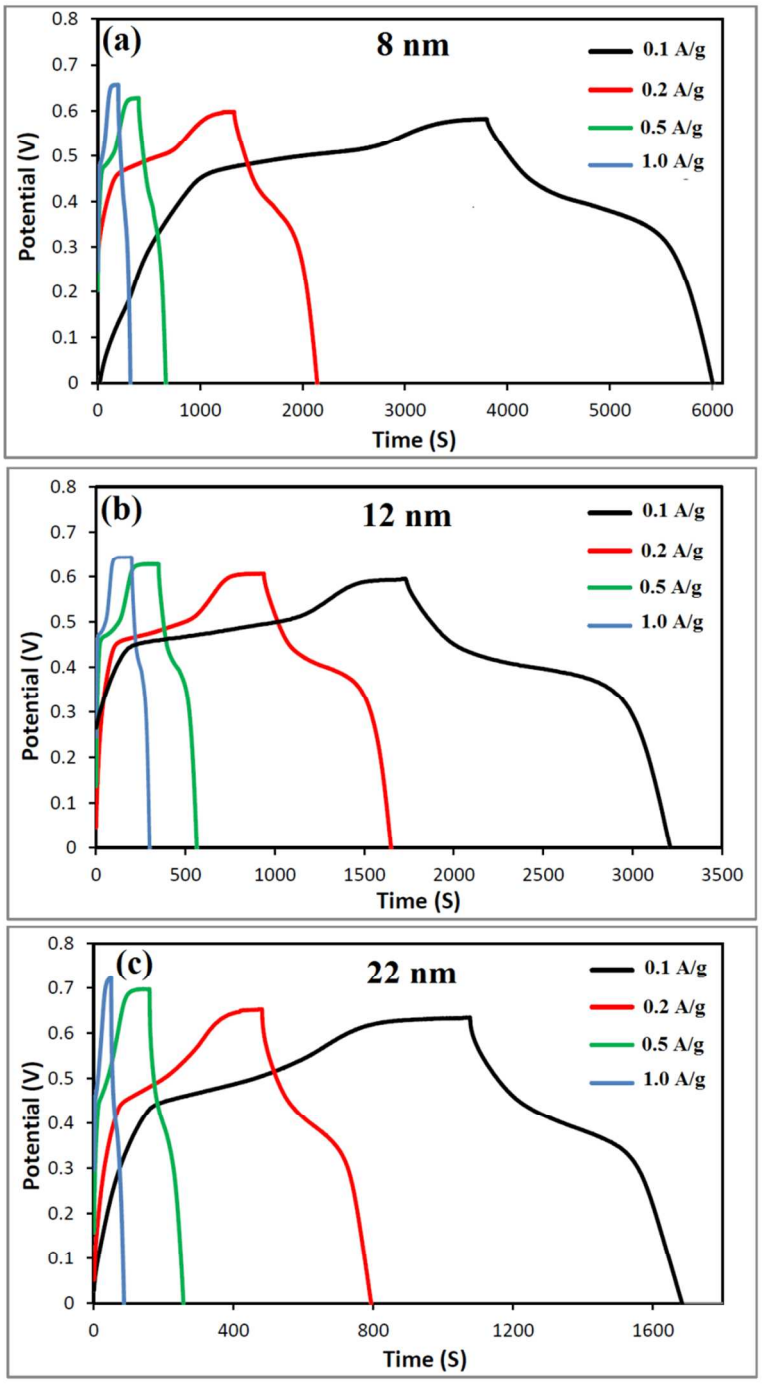

Figure 7. (a-c) The chronopotentiomentery curves of the NiO NPs with particle size of 8, 12, and 22 nm at different current density.

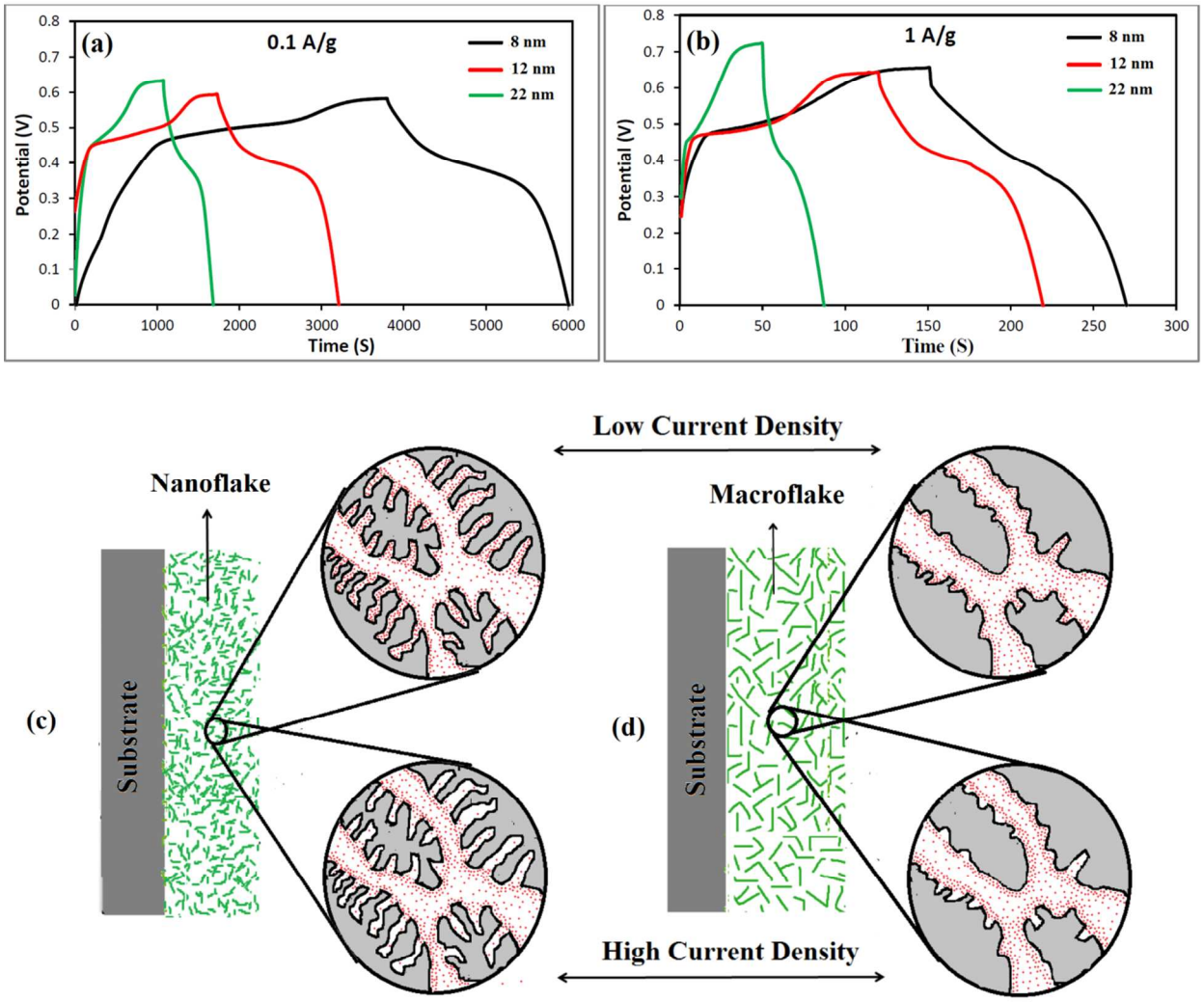

Figure 8. (a-b) The Galvanostatic charge–discharge curves obtained at low and high current density for the NiO NPs with particle size of 8, 12, and 22 nm. (c-d) The schematics of the morphology NiO electrode with different particle size and their effect on the diffusion of electrolyte ions with the NiO electrodes.

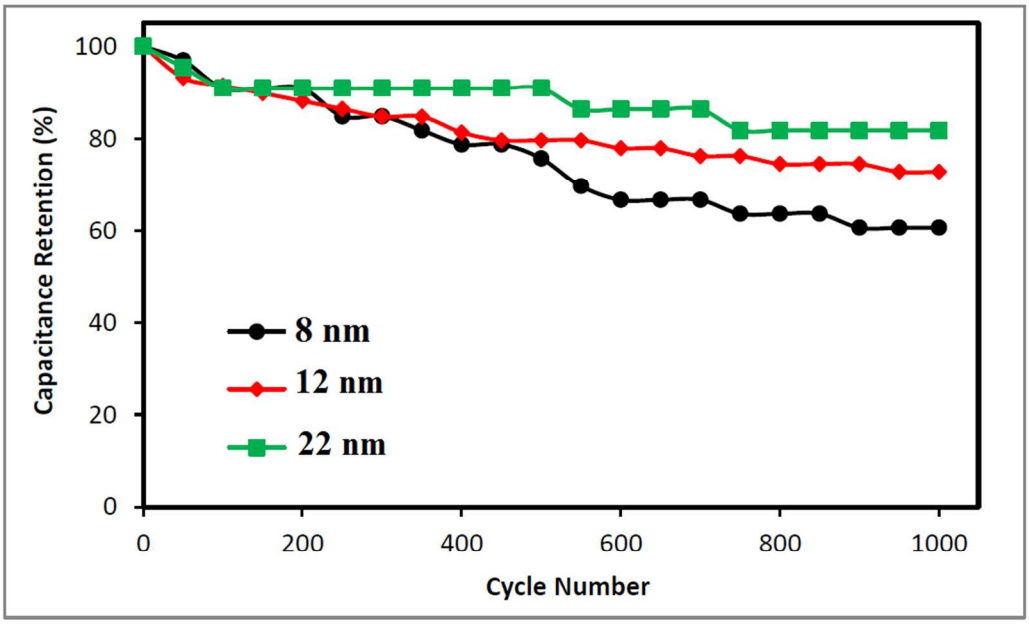

Figure 9. Capacitance retention for the NiO NPs electrode with different particle size.

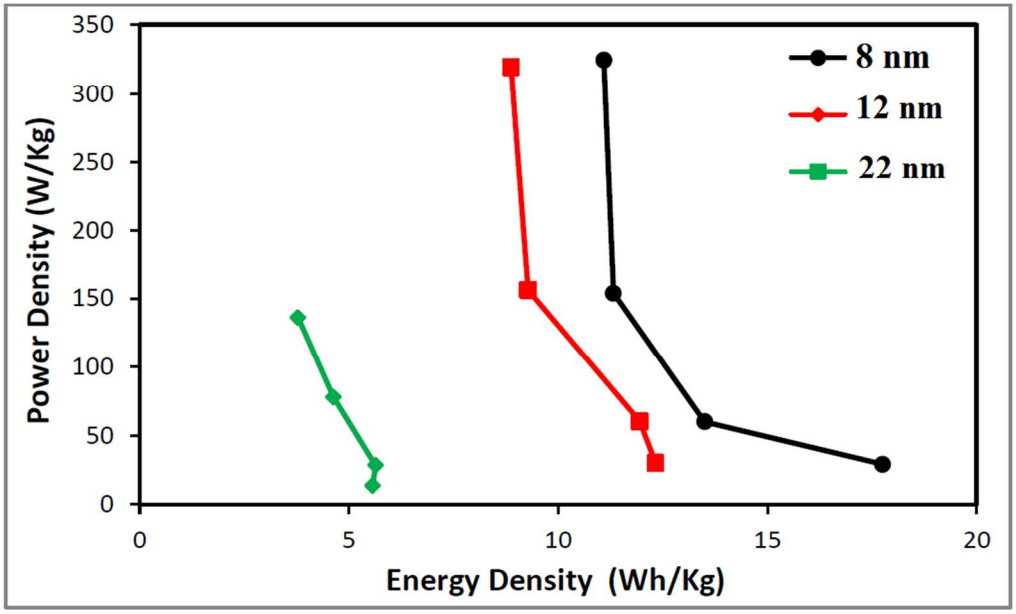

Figure 10. Ragone plots of NiO NPs electrode with different particle size.

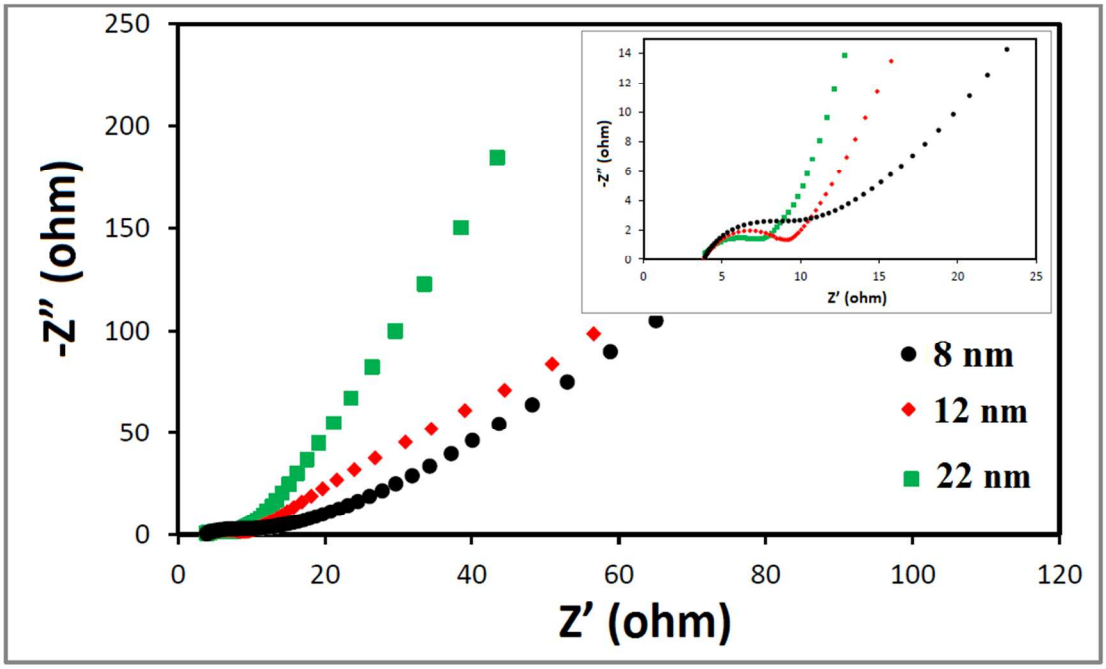

Figure 11. The Nyquist plots of NiO NPs electrode with different particle size.